



PCCP

**Chemical ordering phenomena in nanostructured FePt:
Monte Carlo Simulations**

Journal:	<i>Physical Chemistry Chemical Physics</i>
Manuscript ID:	CP-ART-02-2015-001054.R3
Article Type:	Paper
Date Submitted by the Author:	01-Aug-2015
Complete List of Authors:	Kozubski, Rafal; Jagiellonian University in Krakow, Faculty of Physics, Astronomy and Applied Computer Science Brodacka, Sylwia; Jagiellonian University in Krakow, Faculty of Physics, Astronomy and Applied Computer Science Kozlowski, Mirosław; Jagiellonian University in Krakow, Faculty of Physics, Astronomy and Applied Computer Science Goyhenex, Christine; Institut de Physique et Chimie des Matériaux de Strasbourg, Université de Strasbourg,

SCHOLARONE™
Manuscripts

ARTICLE

Cite this:
10.1039/x0xx00000x

DOI: **Chemical ordering phenomena in
nanostructured FePt: Monte Carlo Simulations**

S. Brodacka^a, M. Kozłowski^a, R. Kozubski^a, Ch. Goyhenex^b, G.E. Murch^c

Received 00th January 2012,
Accepted 00th January 2012

DOI: 10.1039/x0xx00000x

www.rsc.org/

Free-surface-induced L_{1_0} chemical long-range ordering phenomena in a nanolayer, a nanowire and a cubic nanoparticle of FePt were studied by means of Monte Carlo simulations. The system was modeled with nearest-neighbor and next-nearest-neighbor interatomic pair interactions deduced from *ab initio* calculations. The generated samples, the dimensionality of which was determined by appropriate periodic boundary conditions imposed upon the generated supercells, were initially either perfectly ordered in the c-variant L_{1_0} superstructure ((001)-oriented monatomic planes), or completely disordered in the fcc crystalline structure. Vacancy-mediated creation of equilibrium atomic configurations was modelled by relaxing the systems at temperatures below the 'order-disorder' transition point using the Glauber algorithm implemented with the vacancy mechanism of atomic migration. The (100)-type-surface-induced heterogeneous nucleation of L_{1_0} -order domains was observed and quantified by means of an original parameterization enabling selective determination of volume fractions of particular L_{1_0} -variants. Due to the specific competition between the three kinds of (100)-type free surfaces, the initial c- L_{1_0} variant long-range order appeared to be the most stable in the cubic nanoparticle. The initially disordered samples were transformed by the creation of a specific L_{1_0} domain structure with a mosaic of particular L_{1_0} -variant domains at the surfaces and almost homogeneous long-range order in the inner volume. The analysis of correlation effects revealed that chemical ordering was initiated at the free surfaces.

Introduction

Nanostructured $L1_0$ ordered intermetallics such as FePt, FePd, CoPt, have attracted interest for several decades due to their magnetic properties (technology of high density storage media) and to their surface activity (catalysis). In parallel, the intensive development of experimental and computational techniques has enabled the traditional studies of materials to approach the atomistic scale and has opened a wide field for carrying out studies by means of physical methods.

The structural origin of the attractive properties of the alloys (first investigated in thin (nano) films and later in nanoparticles) is their $L1_0$ superstructure (Figure 1). Studies of the effect of nanostructurization (dimensionality, particle shape etc.) on the chemical order have been particularly well developed in this structure.

Figure_1.tiff

Figure 1 Scheme of the $L1_0$ superstructure of FePt: (◻) Fe atoms, (◼) Pt atoms. The (100), (010) and (001) orientations of the sequences of alternate Fe and Pt monatomic planes define the a-, b- and c-variants of the $L1_0$ superstructure.

The related literature of the last decade covers both experimental and theoretical (modeling) papers. Sato et al. [1,2] reported a low degree of $L1_0$ chemical long-range-order (LRO) in 12 nm FePt particles fabricated by electron-beam evaporation and annealed for 24 h at 873 K. The critical size of 2 nm for $L1_0$ ordering of FePt particles was determined by Miyazaki et al. [3], who remarked, however, that because of thermal noise, no magnetic stability should be expected in arrays built from such small particles. A decrease of the degree of LRO with a decrease of FePt particle size was confirmed by Rong et al. [4]. The most recent experimental studies of chemical ordering in nanostructured FePt were devoted to Zn-doped nanowires [5] and to nanoparticles with a diverse Pt concentration [6]. In both cases, the effect of composition on the stability of chemical and magnetic order was investigated.

Effects of $L1_0$ chemical ordering in FePt nanoparticles have been modeled both at the atomistic and mesoscopic scales. Chepulskii et al. [7,8] performed extensive Monte Carlo simulations implemented with interatomic pair potentials

evaluated by way of ab-initio calculations for FePt. The $L1_0$ superstructure was generated even in particles 3.5 nm in size. The superstructure decayed with increasing temperature showing an order-disorder transition of a continuous character. The phenomenon was also observed in the simulations performed later by Yang et al. [9] who concluded that most of the nanostructure-induced effects such as the size dependence of the volume-averaged long-range order parameters and ordering temperatures, as well as the continuous nature of the ordering transition, are due to surface disordering. A considerable contribution to the modeling of ordering phenomena in FePt nanoparticles has been due to Mueller and Albe [10,11], who performed Monte Carlo (MC) simulations of FePt particles modeled with nearest-neighbor (nn) and next-nearest-neighbour (nnn) atomic pair interactions adjusted to the Fe-Pt bulk phase diagram and experiments on surface segregation of FePt thin films. Simulation of particles with regular truncated octahedral shape and with stoichiometric and off-stoichiometric composition revealed a strong effect of surface segregation (in off-stoichiometric samples) on the ordering phenomena [10]. The study was later repeated and extended for initially disordered stoichiometric FePt particles with and without a substrate. The simulations showed that fast nucleation of ordered domains occurred on (100) facets, but was then retarded in the particle volume [11]. In parallel with Mueller and Albe, Li et al. [12] modeled the size-effect on chemical ordering in a series of B2, $L1_0$ and $L1_2$ nanoparticles. Using a Bragg-Williams-type model they showed that the superstructure stability is strongly sensitive not only to the size, but also to the shapes of nanoparticles. Recently, by implementing the MC algorithm with effective classical spin Hamiltonian, Lyberatos et al. [13] found specific finite size scaling relations for the temperature variation of the specific heat and longitudinal susceptibility in FePt nanoparticles.

Regarding the most recent literature in the field, Shuaidi Zhang et al. [14] developed a classical thermodynamic model for the order-disorder transition kinetics in FePt nanoparticles. They found a size limit for ordering and concluded that the elimination of antiphase boundaries considerably hinders the process in nanoparticles. The Phase Field technique was, in turn, used by Yamakawa et al. [15] in the study of the stability of surface composition in various Pt-based alloy nanoparticles considered for application as catalysts in fuel cell technology.

As already mentioned, the attractive magnetic properties (high magnetic anisotropy) of the nanostructured $L1_0$ -ordering intermetallics are strictly correlated with the geometry of their superstructure. The potential key application of the intermetallics in the technology of high density

magnetic storage media depends critically on the preparation of stable nanolayers or nanoparticle matrices showing an *off-plane* direction of the easy magnetization. Thus, the intermetallic nanolayers or nanoparticles should exhibit a stable $L1_0$ chemical long-range order with monatomic planes oriented *in parallel* to the layer/matrix surface. Hence, it is striking that among hundreds of publications devoted to diverse aspects of the effect of nanostructurization on chemical ordering in $L1_0$ intermetallics very few (if any) papers dealt with a question of the orientation (variant) of the generated $L1_0$ superstructure.

The present paper attempts to fill this information gap. It reports on new results of atomistic modelling of the stability and homogeneity of the $L1_0$ superstructure in nanolayers, nanowires and nanoparticles of FePt.

Carrying out extensive atomistic MC simulation studies on chemical ordering kinetics in FePt nanolayers we noticed and described in detail the effect of selective surface-induced destabilization of the $L1_0$ superstructure variants in FePt layers [16-18,20,21]. It was demonstrated that the (100)-type free surfaces limiting the layers destabilize the $L1_0$ superstructure variants with monatomic crystallographic planes of the same orientation – i.e. parallel to the surface. Consequently, a (001)-oriented FePt layer initially homogeneously ordered in the c- $L1_0$ variant (see Figure 1) transforms into a mosaic of a- and b- $L1_0$ variant antiphase domains (APD). In view of the previous remarks, this phenomenon is definitely parasitic from the point of view of magnetic storage technology. Although, after having revealed the effect by simulations, we observed it experimentally in the case of the annealed FePd layers [17] and in the annealed FePt multilayers deposited epitaxially on MgO [19], it has never been reported by other authors investigating theoretically or experimentally the $L1_0$ ordering intermetallics with high magnetic anisotropy.

We showed that the a- and b- $L1_0$ variant APDs nucleated heterogeneously on the (001) free surface of a FePt layer and then grew inward into the material with a specific fluctuating kinetics [18]. The result yielded first by the MC simulation of a *rigid lattice* Ising model of FePt with nn and nnn interatomic pair interactions [16,18] was perfectly reproduced by hybrid Monte Carlo/Molecular Statics (MC/MS) simulations implemented with Analytic Bond Order Potentials (ABOP) dedicated to FePt and accounting for tetragonal distortion effects [20,21].

The above results obtained for FePt layers allowed the anticipation of interesting effects to occur in FePt nanostructures (nanowires and nanoparticles) limited by more than two surfaces. In view of the technological interest not only in magnetic nanolayers, but also in the matrices of nanoparticles it is important to examine the possible influence of

the nanostructure geometry on the stability of the homogeneous $L1_0$ superstructure in FePt.

Methodology

The Monte Carlo (MC) simulations – the tool of the present study, belong to a widely used class of computational algorithms for simulating the behavior of various physical and mathematical systems. They are distinguished from other simulation methods (such as Molecular Dynamics) by being stochastic, that is nondeterministic in some manner. The MC simulations found extremely successful application in statistical thermodynamics providing approximate techniques for the evaluation of macroscopic parameters (observables). This is achieved by means of so called ‘importance sampling’ techniques based on the stochastic theory of Markov chains. The ‘translation’ of the analytical methods of Statistical Thermodynamics into MC techniques was mostly due to Kurt Binder. The references to his numerous works can be found in a recent monograph summarizing the basic ideas and perspectives of Statistical Thermodynamics by MC simulations [22]. In the basic study a cubic supercell of FePt containing $40 \times 40 \times 40$ fcc unit cells (256 000 lattice sites) was generated. The lattice sites were occupied by equal numbers of Fe and Pt atoms either arranged in a perfect c-variant $L1_0$ superstructure (Figure 1), or distributed at random.

A bulk sample and particular nanostructures of FePt were simulated by imposing specific Periodic Boundary Conditions (PBC) upon the supercell – as shown in Table 1.

Table 1 Geometries of PBC imposed on the supercells to generate particular FePt nanostructures

Sample	PBC
bulk	3D PBC in [100], [010] and [001] directions
(001)-oriented 40 unit cell (ca. 15 nm) – thick nanolayer	2D PBC in [100] and [010] directions Figure_table1a.tiff
[100]-oriented 40×40 unit cell (ca. $15 \times 15 \text{ nm}^2$) – thick nanowire	1D PBC in [100] direction Figure_table1b.tiff
Ca. $15 \times 15 \times 15 \text{ nm}^3$ nanocube built of $40 \times 40 \times 40$ fcc unit cells	No PBC Figure_table1c.tiff

The lattice sites of the supercells were occupied by equal numbers of Fe and Pt atoms either arranged in a perfect c-variant $L1_0$ superstructure (Figure 1), or distributed at random.

A single vacancy was introduced in the supercell by emptying a lattice site selected at random. An Ising-type model of the FePt system was applied with fixed

nn and nnn pair-interaction energies evaluated from *ab initio* calculations and used in our previous papers [16-19] (Table 2).

Table 2 nn and nnn pair interaction energies in FePt [16].

Interacting atoms	nn interaction energy [meV]	nnn interaction energy [meV]
Fe-Fe	11.45	-1.145
Fe-Pt	-67.05	6.705
Pt-Pt	85.63	-8.563

In order to test the size effect on the simulated properties a (001)-oriented 80 unit cell (ca. 30 nm) -thick nanolayer, (001)-oriented 20 unit cell (ca. 7.5 nm) -thick nanolayer, [100]-oriented 20×20 unit cell (ca. 7.5×7.5 nm²) -thick nanowire and ca. 7.5×7.5×7.5 nm³ nanocube built of 20×20×20 fcc unit cells were also examined. The samples were simulated by imposing PBC of Table 1 on 20 (80) unit cell – thick supercells, which in the case of both nanolayers and the nanowire were cuboidal in order to contain 256 000 lattice sites (similarly as in the case of the thicker samples). The nanocube (simulated with a cubic supercell) contained 32 000 lattice sites. In the following, the 40-unit-cell-thick and 20-unit-cell-thick samples are referred to as ‘thick’ and ‘thin’ samples, respectively.

Quasi-equilibrium atomic configurations of the systems corresponding to $T/T_T = 0.76, 0.83, 0.89, 0.95$, where T is the current temperature and $T_T = 1575$ K denotes the order-disorder $L1_0 \rightarrow A1$ transition temperature simulated for the bulk FePt, as well as their MC-time isothermal evolution were simulated by means of the Glauber MC algorithm assuming atomic jumps performed exclusively to nn vacancies in the *rigid fcc lattice*. A single MC step consisted of (i) random selection of one particular atom among the nearest neighbors of the vacancy and (ii) execution or rejection of its jump to the vacancy according to the probability Π equal to:

$$\Pi = \exp\left[-\frac{\Delta E}{k_B T}\right] / \left(1 + \exp\left[-\frac{\Delta E}{k_B T}\right]\right)$$

Equation 1

where ΔE denotes the change of the system configurational energy due to the jump, k_B and T denote the Boltzmann constant and absolute temperature, respectively.

Such a probability obeys so-called ‘detailed balance’ principle which makes it sure that the system evolves towards the equilibrium atomic configuration [22].

Equal numbers of atoms in the supercells enabled comparison of the results obtained for different samples within the same MC time. Only in the case of the ‘thick’ and ‘thin’ nanocubes, comparison of the results required that MC time was rescaled proportionally to their sizes.

The atomic configurations resulting from the simulations were quantitatively analysed by monitoring two sets of parameters:

- the LRO parameters η_α defined for particular α -L1₀ superstructure variants and varying from 1 (perfect order in the α -L1₀ variant) to 0 (random distribution of atoms or perfect order in another L1₀ variant). The η_α parameters were evaluated for particular parts of the nanostructures (inner volumes, surface areas, edges and vertices). In order to minimize the effect of possible L1₀ antiphase domains within the particular L1₀ variant areas the η_α parameters were calculated in cubes built of 2×2×2 fcc unit cells and then averaged over the number M of the cubes contained in particular nanostructure parts:

$$\eta_\alpha = \frac{1}{M} \times \sum_{i=1}^M \left| 2 \times \frac{N_{Pt,j}^{(Pt_\alpha)}}{N^{(Pt_\alpha)}} - 1 \right|$$

Equation 2

where $N_{Pt,i}^{(Pt_\alpha)}$ denotes the number of Pt atoms occupying the Pt sublattice sites of the i -th cube in the α -L1₀ variant; $N^{(Pt_\alpha)}$ denotes the number of Pt sublattice sites in a cube in the α -L1₀ variant (obviously $N^{(Pt_\alpha)} = 16$). It should be noted that the applied 2×2×2 cubes are the smallest ones in which a random distribution of atoms yields $\eta_\alpha = 0$ for each L1₀ variant.

In the case of the coexistence of domains ordered in different L1₀ variants the values of particular η_α parameters do not yield the degree of LRO, but rather reflect the volume fractions γ_α of the variant domains. As it is reasonable to assume that at a given temperature the equilibrium degree of LRO is the same within each L1₀ variant, the following approximation holds:

$$\gamma_\alpha = \frac{\eta_\alpha}{\sum_i \eta_i}$$

Equation 3

- nn pair correlation parameters associated with particular α -L1₀ variants and calculated in single (hkl)-oriented crystallographic planes:

$$\rho_\alpha^{(hkl)} = \frac{N_{FeFe}^{[\alpha,(hkl)]}}{2 \times N_{Fe}^{[Fe,\alpha,(hkl)]}}$$

Equation 4

where: $N_{Fe}^{(Fe,\alpha,(hkl))}$ denotes the number of Fe atoms located on the (hkl) crystallographic plane and occupying Fe-sublattice-sites corresponding to the α -L1₀ variant; $N_{FeFe}^{(\alpha,(hkl))}$ denotes the number of nn Fe-Fe pairs selected as follows: one of the Fe atoms belongs to the $\{N_{Fe}^{(Fe,\alpha,(hkl))}\}$ set, the other one is its nearest neighbor on the (100) plane for $\alpha=a$, the (010) plane for $\alpha=b$ and the (001) plane for $\alpha=c$.

The values of $\rho_{\alpha}^{(hkl)}$ corresponding to extreme (fully disordered and fully ordered) atomic configurations are displayed in Table 3:

Table 3 $\rho_{\alpha}^{(hkl)}$ values corresponding to extreme atomic configurations in the fcc crystalline lattice.

	Disorder-random distribution of atoms	a-L1 ₀ variant LRO	b-L1 ₀ variant LRO	c-L1 ₀ variant LRO
$\rho_a^{(100)}$	2	4	0	0
$\rho_a^{(010)}$	1	4	0	0
$\rho_a^{(001)}$	1	4	0	0
$\rho_b^{(100)}$	1	0	4	0
$\rho_b^{(010)}$	2	0	4	0
$\rho_b^{(001)}$	1	0	4	0
$\rho_c^{(100)}$	1	0	0	4
$\rho_c^{(010)}$	1	0	0	4
$\rho_c^{(001)}$	2	0	0	4

Unlike other papers (see e.g. [9]), in the present work the interest was focused on the formation/decay and possible interplay between particular L1₀ variant domains and accordingly, the η_{α} and $\rho_{\alpha}^{(hkl)}$ parameters were analysed individually.

The studies were performed within two principal simulation cycles:

- Disordering runs: the initial atomic configuration of the simulated samples corresponded to the perfect chemical order in the c-L1₀ variant ($\eta_a = \eta_b = 0$, $\eta_c = 1$, $\rho_a^{(hkl)} = \rho_b^{(hkl)} = 0$, $\rho_c^{(hkl)} = 4$) and simulated was the process of disordering at

four temperatures below T_T (see the previous section).

- Ordering runs: the initial atomic configuration of the simulated samples corresponded to total chemical disorder (a random distribution of Fe and Pt atoms, ($\eta_{\alpha} = 0$, $\rho_{\alpha}^{(hkl)} = 1(2)$) and the process of ordering was simulated at the same temperatures as in the previous case. More than in the previous case, of interest was the kinetics of ordering – i.e. the MC-time evolution of the L1₀ domain structure of the samples.

The equivalence of the formation of particular L1₀ variants (a- and b-variants from the initial c-variant and any on the a-, b- and c-variants from the disordered fcc structure) often resulted in the cancelling-out of the effects of interest when averaging the parameter values over independent simulation runs. This is why the results of single simulation runs were mainly analysed and averaging (over 30 simulation runs) was performed only for checking the above equivalence in particular cases.

In the following sections, graphs presenting the quantitative results of the simulations are illustrated by images directly showing the atomic configurations of a quarter of (100) section in the middle of the supercell body and of a quarter of the (001) oriented free surface.

Results

Disordering simulation runs

General properties.

Figure 2 shows representative examples of the atomic configurations generated by 10^{10} MC steps in the simulated ‘thick’ nanolayer, nanowire and nanoparticle of FePt at $T/T_T = 0.95$.

Image type	(100)-oriented cross section	(001)-oriented free surface
Initial configuration: $\eta_a = \eta_b = 0, \eta_c = 1$		
Each sample	Figure_2_a.tiff	Figure_2_b.tiff
After 10^{10} MC steps at $T/T_T = 0.95$		
nanolayer	Figure_2_c.tiff	Figure_2_d.tiff
nanowire	Figure_2_e.tiff	Figure_2_f.tiff
nanocube	Figure_2_g.tiff	Figure_2_h.tiff

Figure 2 Atomic configurations in the 'thick' samples initially ordered in the c-L1₀ variant and annealed for 10¹⁰ MC steps at $T/T_T = 0.95$. Black and white dots represent Fe and Pt atoms, respectively. For the sake of better legibility of the pictures only quarters of the sample cross sections and surfaces are displayed.

The images should be interpreted by comparing the atomic configurations with the initial ones (first row) corresponding to the ideal LRO in the c-L1₀ variant. It can be seen that 'regular' disordering (homogeneous generation of antisite defects) proceeded in parallel with heterogeneous nucleation and growth of a- and b-L1₀ variant domains on the (001) free surfaces. The effect is the most clearly reflected by the definite change of the configuration of the originally monatomic (001) surfaces of the samples. No particular nucleation and growth effects were observed on surfaces with other orientations. Further quantitative analysis of the sample configurations was, therefore, done separately within their inner and surface-affected parts. The first step was the evaluation of the average widths of the surface-affected parts (determining their sizes) by analyzing the profiles of $\rho_{\alpha}^{(hkl)}$ pair correlations (Equation 4). An example of such profiles determined for the three FePt nanostructures is shown in Figure 3

Figure_3.tiff

Figure 3 Profiles of $\rho_c^{(001)}$ calculated in the consecutive (001) planes in the nanocube annealed for 10¹⁰ MC steps at: $T/T_T = 0.76$ (▲), $T/T_T = 0.83$ (◀), $T/T_T = 0.89$ (◐) and $T/T_T = 0.95$ (⊗).

According to Table 3 the well-marked edges of $\rho_c^{(001)}$ close to the free surfaces reflect the penetration depth (PD) of the growing domains of a- and b-L1₀ variants.

Figure 4 shows the temperature dependence of the average PD determined in the above way for particular nanostructures after 10¹⁰ MC steps.

Figure_4.tiff

Figure 4 Temperature dependence of the growing domain penetration depth PD in the simulated FePt nanostructures: 'thick' (▲) and 'thin' (◀) nanolayer; 'thick' (◐) and 'thin' (⊗) nanowire; 'thick' (◀) and 'thin' (⊗) nanocube.

The results shown in Figure 4 indicate that the PD of the growing a- and b-L1₀ variant domains was the lowest in both FePt nanocubes. This means that a large fraction of their volumes was still ordered in the c-L1₀ variant (with η_c decreased due to homogeneous generation of antisite defects). There was no significant size (thickness) effect on the values of PD. At $T/T_T = 0.95$, however, the PD in the 'thin' nanolayer and nanowire approached the sample thickness, which meant the transformation of the entire samples (Figure 5).

nanolayer	nanowire	nanocube
Figure_5_a.tiff	Figure_5_b.tiff	Figure_5_c.tiff

Figure 5 Atomic configurations of the (100) cross sections of the 'thin' samples initially ordered in the c-L1₀ variant and annealed for 10¹⁰ MC steps at $T/T_T = 0.95$. Black and white dots represent Fe and Pt atoms, respectively.

Stability of the atomic configurations of the samples.

As only the inner parts of all the samples remained homogeneously ordered in the c-L1₀ variant the configuration stabilization in the annealed samples was checked by monitoring the MC-time dependence of the LRO parameter η_c in the inner parts and of the c-variant volume fraction γ_c in the PD-thick surface-affected parts of the samples. The corresponding graphs are available in the ESI‡.

While the configurations of the inner parts of all the samples were almost stable after 10^{10} MC steps, a continuous linear-like evolution of the $L1_0$ -variant domain structure was still observed in the surface-affected parts of the nanolayer and nanowire. Remarkably, the FePt nanoparticle (nanocube) that exhibited the lowest PD of the growing domains of a- and b- $L1_0$ variants showed good stability of the atomic configuration in the entire volume.

Figure 6 shows the temperature dependences of the values of η_c in the inner parts of the ‘thick’ samples after 10^{10} MC steps.

Figure_6.tiff

Figure 6 Temperature dependences of the values of η_c in the inner part of the ‘thick’ nanolayer (⊗), ‘thick’ nanowire (⊕) and ‘thick’ nanocube (⊖) after 10^{10} MC steps.

The ideal coincidence of all the three dependences shows that the processes running in the surface-affected parts of the examined nanostructures had negligible influence on the chemical long-range ordering in the inner parts.

Analysis of the $L1_0$ -variant domain structure. A more detailed analysis of the atomic configurations of the samples after 10^{10} MC steps consisted of the determination of the volume fractions γ_x of the particular $L1_0$ variant domains (Equation 3) within the characteristic surface-affected areas of the samples (Table 4).

Table 4 Specification of the selectively analysed surface-affected areas of the simulated FePt samples

sample	Characteristic areas analysed for LRO in particular $L1_0$ variants
nanolayer	PD-thick layer adjacent to the (001) surface; inner part - central layer;
nanowire	PD-thick layer adjacent to the (001) surface; PD-thick layer adjacent to the (010) surface; [100] oriented PD×PD edge area; inner part - [100]-oriented central core
nanocube	PD-thick layer adjacent to the (100) surface; PD-thick layer adjacent to the (010) surface; PD-thick layer adjacent to the (001) surface; [100] oriented PD×PD edge area [010] oriented PD×PD edge area [001] oriented PD×PD edge area PD×PD×PD (111) vertex area inner part - central core

An example of the resulting graphs corresponding to the ‘thick’ samples is shown in Figure 7 (the full set of the graphs may be found in the ESI ‡)

Figure_7.tiff

Figure 7 Temperature dependence of the $L1_0$ -variant volume fractions γ_x in a single sample of the ‘thick’ nanowire. Inner part: γ_a (⊗), γ_b (⊕), γ_c (⊖); layer adjacent to the (010) surface: γ_a

(⊗), γ_b (⊕), γ_c (⊖); layer adjacent to the (001) surface: γ_a (⊗), γ_b (⊕), γ_c (⊖); [100] oriented edge area: γ_a (⊗), γ_b (⊕), γ_c (⊖).

The volume fractions γ_x of the particular $L1_0$ -variant domains in the surface affected areas were almost independent of temperature. In the case of the [100]-oriented nanowire (Figure 7) the a-variant domains (with (100)-oriented monatomic planes perpendicular to both (010)- and (001)-oriented surfaces) markedly dominated at $T/T_T < 0.95$ in the areas adjacent to the (001) free surface. On the other hand, the initial c-variant clearly dominated in the surface-affected areas of both the nanolayer and the nanocube - apparently due to the PD being associated with the edge of $\rho_\alpha^{(hkl)}$ (Figure 3) - and not with, for example, the position where it is reduced by 50%. The a- and b-variant domains with non-negligible volume fractions were observed in all the areas adjacent to the (001) surface (Table 4). Remarkably, while one of the a- and b-variant domains always definitely dominated in particular samples, the values of γ_a and γ_b averaged over 30 independent simulation runs resulted in being almost equal.

Sample volumes that were remote from the (001) free surface remained untransformed and still ordered in the c- $L1_0$ variant.

The initial c-variant $L1_0$ superstructure of the cube was favoured by both the (010) and the (100) free surfaces, which were thus free of any transformation. In general, the c- $L1_0$ variant LRO dominated with $\gamma_c > 60\%$ in all parts of the nanocube. The volume fractions of the remaining $L1_0$ variant domains never exceeded 30%.

The volume fractions γ_c of the $L1_0$ c-variant domains calculated for the entire volumes of all the three FePt nanostructures after 10^{10} MC steps are traced in Figure 8. It is clear that the nanocube sample shows the highest γ_c over the entire temperature range.

Figure_8.tiff

Figure 8 Temperature dependence of the $L1_0$ -variant volume fractions γ_x calculated for the entire sample volume. γ_a : (⊗)-nanolayer, (⊕)-nanowire, (⊖)-nanocube; γ_b : (⊗)-nanolayer, (⊕)-nanowire, (⊖)-nanocube; γ_c : (⊗)-nanolayer, (⊕)-nanowire, (⊖)-nanocube.

The $L1_0$ -variant domain structures generated in the ‘thin’ samples by 10^{10} MC steps (10^9 MC steps in the case of the ‘thin’ nanocube) at $T/T_T < 0.95$ were similar to those observed in the ‘thick’ samples. In agreement with Figure 5, the ‘thin’ nanolayer and nanowire contained no c- $L1_0$ variant domains ($\gamma_c = 0$) after 10^{10} MC steps at $T/T_T = 0.95$.

We checked for a possible effect of the geometry and size of the examined nanostructured samples on the atomic configuration of their (001) free surfaces. The

values of γ_x after 10^{10} MC steps at $T/T_T = 0.95$ were additionally calculated within the 2 fcc unit-cell-thick layers adjacent to the (001) surfaces. Except for the ‘thick’ and ‘thin’ samples, the 80 fcc-unit-cell-thick layer was also examined as approximating a surface-limited bulk. The results displayed in Figure 9 indicate that while the nanostructure *geometry* definitely affected the (001) free surface configuration, no size effect was observed.

Figure_9.tiff

Figure 9 $L1_0$ -variant domain structures of the (001) surfaces of the examined FePt nanostructures after 10^{10} MC steps at $T/T_T = 0.95$: γ_a (⚡, ⚡); γ_b (⚡, ⚡); γ_c (⚡, ⚡). Solid and open symbols correspond to the ‘thick’ and ‘thin’ samples, respectively. The values of γ_x were obtained by single simulation runs.

In the case of the nanolayers and the nanowires, the (001) surfaces showed a high degree of LRO in one of the a- and b- $L1_0$ -variants. While particular (a- or b-) $L1_0$ variants appeared at random in the case of nanolayers, the [100] orientation of the nanowire definitely forced the a- $L1_0$ variant LRO on the (001) free surface. In contrary to the nanolayers and nanowires, the (001) free surface of the nanocube showed a mosaic pattern of domains of all the three $L1_0$ variants.

Ordering simulation runs

Atomic ordering starting from initially disordered FePt samples was simulated exclusively at $T/T_T = 0.95$. Images of atomic configurations generated in the ‘thick’ samples by 10^{10} MC steps (Figure 10) show well-marked $L1_0$ -variant domain structures with statistically distributed antisite defects. The domain structure was specific for the particular sample geometries and clearly influenced by free surfaces.

In no case was the (001) free surface monatomic. This indicates a- or b- $L1_0$ LRO at this surface. The configurations of the (100) supercell sections showed a single $L1_0$ variant LRO disrupted in the vicinity of the surfaces. The large single $L1_0$ -variant areas were, however, inhomogeneous and contained antiphase domains – as clearly shown in the case of the nanowire.

Quantitative analysis of the results was carried out by calculating the $L1_0$ -variant volume fractions γ_x within a sequence of converging shells defined specifically for the simulated FePt nanolayer, nanowire and nanocube (Table 5).

Image type	(100)-oriented cross section	(001)-oriented free surface
Initial configuration: $\eta_a = 0$		
Each sample	Figure_10_a.tiff	Figure_10_b.tiff
After 10^{10} MC steps at $T/T_T = 0.95$		
nanolayer	Figure_10_c.tiff	Figure_10_d.tiff
nanowire	Figure_10_e.tiff	Figure_10_f.tiff
nanocube	Figure_10_g.tiff	Figure_10_h.tiff

Figure 10 Atomic configurations in initially disordered ‘thick’ samples annealed for 10^{10} MC steps at $T/T_T = 0.95$. Black and white dots represent Fe and Pt atoms, respectively. For the sake of better legibility of the pictures only quarters of the sample cross sections and surfaces are displayed.

Table 5. Geometry of shells defined for the sake of the analysis of chemical ordering in initially disordered FePt nanostructures. An image of the shells in the nanowire is displayed.

Sample	Shell geometry
layer	Converging consecutive pairs of two-unit-cell-thick coaxial layers parallel to the free surfaces – enumeration starts from the surfaces
wire	Figure_table_5.tiff Converging consecutive two-unit-cell-thick coaxial shells oriented along the wire [100] axis – enumeration starts from the surfaces
cube	Converging consecutive two-unit-cell-thick concentric cubic shells – enumeration starts from the surfaces

Figures 11a-c show the volume fractions γ_x in the consecutive shells of the samples (Table 5) after 10^{10} MC steps at $T/T_T = 0.95$. The data corresponding to single simulation runs are presented together with those averaged over 30 independent ones.

a)

Figure_11_a.tiff

b)

Figure_11_b.tiff

c)

Figure_11_c.tiff

Figure 11 $L1_0$ -variant volume fractions γ_x against the consecutive shell numbers in the initially disordered ‘thick’ FePt nanolayer (a), nanowire (b) and nanocube (c) annealed for 10^{10} MC steps at $T/T_T = 0.95$. γ_a : (♣)-single sample, (♣̄)-averaged; γ_b : (⊖)-single sample, (⊖̄)-averaged; γ_c : (⊞)-single sample, (⊞̄)-averaged.

While one particular $L1_0$ variant domain definitely predominated in the inner volume of each sample, the contribution of other variants markedly increased close to the free surfaces (This is in agreement with the images shown in Figure 10). The systems definitely ‘avoided’ ordering in $L1_0$ variants with monatomic planes parallel to the free surfaces. This resulted in the elimination of the c-variant in the layer (Figure 11a) and of the c- and b-variant in the [100] oriented wire (Figure 11b). No clear preference of the variants was observed in the cube (Figure 11c) – as follows from the difference between the values of γ_x determined with and without averaging over the independent simulation runs. Despite appearing at random, the inner α - $L1_0$ variant domains showed almost the same value of $\eta_\alpha \approx 0.84$ – somewhat lower (apparently due to $\gamma_\alpha < 1$) than the value of η_c estimated in the inner volumes of the samples initially ordered in the c- $L1_0$ variant and annealed at $T/T_T = 0.95$ (Figure 7).

The MC time evolution of the $L1_0$ -variant domain structure was studied for the initially disordered nanocube at $T/T_T = 0.95$. Assuming that each $L1_0$ variant shows similar LRO kinetics and,

consequently, Equation 3 is valid even before equilibrium is reached, the MC-time dependence of γ_α was monitored in the nanocube shells (Figure 12 (from a single simulation run)).

Figure_12.tiff

Figure 12 $L1_0$ -variant volume fractions γ_x against consecutive shell numbers and MC time in initially disordered single ‘thick’ FePt nanocube: (♣) γ_a ; (⊖) γ_b ; (⊞) γ_c .

Figure_13.tiff

Figure 13 $L1_0$ -variant volume fractions γ_x against consecutive shell numbers in initially disordered ‘thick’ FePt nanocube. Data averaged over 30 independent simulation runs: (♣̄) γ_a ; (⊖̄) γ_b ; (⊞̄) γ_c .

While long range atomic ordering in almost one $L1_0$ -variant domain developed after about 10^8 MC steps inside the nanocube, the volume adjacent to the free surfaces (most external shells) was still composed of roughly equi-sized domains of all the three $L1_0$ variants. Nearly equal volume fractions of all the $L1_0$ -variant domains resulted from averaging the results of Figure 12 over 30 independent simulation runs (Figure 13). This indicates the equivalence of the variants developing inside the cube.

The same study was performed for the initially disordered ‘thin’ FePt nanostructures. No particular size effect on the ordering phenomena was observed: the images of atomic configurations on the (001) free surfaces and the (100)-oriented sections, as well the γ_x distribution over the converging shells were similar to those observed in the case of the ‘thick’ samples.

$L1_0$ domain structure of the *entire* surfaces of the initially disordered samples corresponded to the configuration of the external shells (Table 5). The results obtained for both ‘thick’ and ‘thin’ samples are displayed in Figure 14.

Figure_14.tiff

Figure 14 L1₀-variant domain structures of the entire surfaces of the initially disordered FePt nanostructures after 10¹⁰ MC steps at T/T_T = 0.95: γ_a (♣, ♠, ♠); γ_b (♣, ♠, ♠); γ_c (♣, ♠, ♠). Solid and open symbols correspond to the 'thick' and 'thin' samples, respectively. The values of γ_x were obtained by single simulation runs.

Similarly as in the case of the samples initially ordered in the c- L1₀ variant, the surface configurations of the initially disordered samples were clearly affected by the nanostructure geometry, but showed no size effect. The free surfaces of the nanolayers and nanowires were homogeneously ordered in the L1₀ variants with monatomic planes oriented in perpendicular. Again, while the nanowire surface was always ordered in the a-L1₀ variant, random appearance of the a- and b-variants was observed in the nanolayers. As such configurations were not feasible in the case of the nanocube, its surface showed a contribution of other L1₀ variants. It is interesting to remark that the monatomic planes of one particular L1₀ variant are always oriented in perpendicular to four (of the six) surfaces of a nanocube. This is why one particular variant always effectively dominated in the external shell of the nanocube – as visible in Figure 14.

In the final step of the present study, the homo/heterogeneity of L1₀ ordering in the cube and the possible role of the free surfaces as nucleation sites for L1₀ domains was investigated. The investigation was performed by calculating the MC-time-dependent $\rho_\alpha^{(hkl)}$ parameters (Equation 4) in three sequences of (100)-, (010)- and (001)-oriented crystallographic planes stacked in [100]-, [010]- and [001]-oriented 'chimneys' ranging throughout the cube (Figure 15).

Figure_15.tiff

Figure 15 [010]-oriented 'chimney': area for the calculation of $\rho_\alpha^{(010)}$ traced in Figure 16.

The geometry of the 'chimneys' eliminated the influence of the parallel cube surfaces, so that only an effect of surfaces perpendicular to the 'chimney' axis was observed. Figure 16 shows an example of the early-stage MC-time evolution of $\rho_\alpha^{(hkl)}$ corresponding to the subsequent planes stacked inwards the cube starting from the surface.

It is clearly visible that the gradual decrease of $\rho_b^{(010)}$ from the level of 2 (disordered fcc structure) towards lower values (ordering in the a- or c-L1₀ variant) was the fastest in the vicinity of the (010) surface of the cube. Similar results were obtained for the remaining 'chimney' orientations and L1₀ variants, which shows that the L1₀-domains nucleated preferentially on the free surfaces of the simulated cube. In addition, systematic decrease of $\rho_a^{(100)}$, $\rho_b^{(010)}$ and $\rho_c^{(001)}$ below the level of 2 signalises the nucleation and growth of L1₀ variant

domains with monatomic planes perpendicular to the surfaces of nucleation (in agreement with the previous results).

Figure_16.tiff

Figure 16 $\rho_b^{(010)}$ in initially disordered single FePt nanocube against the numbers of consecutive (010)-planes in the [010]-oriented 'chimney' shown in Figure 15. (♣) 10⁴ MC steps, (♠) 10⁵ MC steps, (♠) 5×10⁵ MC steps, (♠) 10⁶ MC steps, (♠) 10⁷ MC steps.

Discussion and Conclusions

The effect of (100)-oriented-free-surface-induced destabilization of L1₀ superstructure variants with monatomic planes parallel to the surface and the nucleation and growth of the L1₀-variant domains with monatomic planes perpendicular to the surface was previously observed and described for the case of a FePt layer [16-21]. The phenomenon was now simulated in FePt nanostructures showing three different geometries (dimensionalities): a nanolayer (2D) limited by (001)-oriented free surfaces, a [100]-oriented FePt nanowire (1D) limited by (010)- and (001)-oriented free surfaces and a nanocube limited by (110), (010) and (001) free surfaces. The samples were modeled with an Ising approximation with nn and nnn pair interactions in a rigid fcc lattice.

It is essential to note that the findings yielded initially by MC simulations [16] and undoubtedly being of great importance for the magnetic storage technology were later on confirmed by experimental observations in FePd [17] and FePt [19] layers. Detailed analysis [21] revealed that the phenomenon is attributed not only to the FePd and FePt layers, but its occurrence is presumed in all AB binaries ordering in the L1₀ superstructure and limited by (100)-type free surfaces. It originates from the difference between the configurational energies $E_{par}^{(surf)}$ and $E_{perp}^{(surf)}$ of (100)-type free surfaces ordered in L1₀ variants with the A- and B-monatomic planes (see Figure 1) oriented either in parallel, or in perpendicular to the surface, respectively. As follows from the calculations performed within the Ising model [21], with ABOP potentials [21], as well as from the *ab initio* calculations [23], perpendicular orientation of the monatomic planes with respect to the surface is energetically favourable:

$$\Delta E^{(surf)} = E_{perp}^{(surf)} - E_{par}^{(surf)} < 0$$

Equation 5

Within the Ising model (which is applied in the present paper) $\Delta E^{(surf)}$ is proportional to the

ordering energy in the 1st co-ordination zone (there is no effect of the nnn pair interactions):

$$\Delta E^{(surf)} \sim 2V_{AB}^{(nn)} - V_{AA}^{(nn)} - V_{BB}^{(nn)}$$

Equation 6

where $V_{ij}^{(nm)}$ denote nn pair interactions between i and j atoms.

While the energy gain (Equation 5) stimulates nucleation of the favourable L1₀-variant domains at particular surfaces the corresponding total change $\Delta E^{(tot)}$ of the configurational energy equals, however, a sum of $\Delta E^{(surf)}$ and the positive energy $\Delta E^{(APB)}$ of the generated antiphase boundaries (APB) between the growing L1₀-variant domains and the matrix. An idealized case of a flat a-variant/c-variant APB in FePt was analysed within the Ising model [18,21]. It was shown that the applied pair potentials (Table 1) yield $\Delta E^{(tot)} < 0$ provided that the surface is initially occupied by Fe atoms.

Hybrid off-lattice MC/MS simulations with ABOP potentials dedicated to FePt [20,21] confirmed the results obtained by means of rigid lattice MC simulations implemented with fixed nn and nnn atomic pair interactions [16-18]. It is remarkable that although the ordering phenomena simulated by the off-lattice MC/MS technique were accompanied by lattice strains (caused predominantly by tetragonal distortions in the particular L1₀-variant domains), the principal features of the processes resulted similar to those observed in the rigid-lattice approach. The only difference was that $\Delta E^{(tot)} < 0$ resulted at surfaces initially occupied by Fe, *as well as* by Pt atoms.

The above findings justified a return to the simple and more efficient technique in the present work.

A new original statistical method for data analysis allowed selective monitoring of nucleation, growth and the evolution of nanodomains of particular L1₀ superstructure variants, as well as the localization of the processes in the sample volume.

The two cycles of the simulations addressed two kinds of processes occurring in real FePt nanostructures: (i) the structure evolution when annealing samples initially homogeneously ordered in the c-L1₀ variant; (ii) the creation of a L1₀-type superstructure when annealing the completely disordered samples.

In the first case, it was demonstrated that the free (100)-type surfaces generally weakened the initial homogeneous c-variant L1₀ long range atomic order. Domains of the energetically favorable L1₀ variants nucleated and grew on the surfaces, but the resulting domain structure of the sample volume adjacent to the surface was specific for the geometries of particular samples.

The observed phenomena were controlled by three factors:

- The energetic unfavorability of the initial c-L1₀ variant LRO
- The energetic favorability of other L1₀ variants
- Reduction of the APB density (both between the domains of different variants and between the antiphase domains within particular variants).

While the first two factors address the free surface geometry, the last one reflects a general tendency.

Nanolayer: Total unfavorability of the c-L1₀ variant LRO (due to two (001)-oriented surfaces) and full equivalency of the a- and b-variants led to a mosaic pattern of the a- and b-variant domains growing inward and finally percolating the layer (see Figure 5 and our previous results [16]). Finally, the layer evolved towards the monodomain LRO (low APB density) in a- or b-L1₀ variant [18].

Nanowire: The c-L1₀ variant was unfavourable for two of four free surfaces. On the other hand, the a-variant was definitely preferable for all free surfaces and thus, the wire evolved towards the monodomain LRO (low APB density) in a-L1₀ variant.

Nanocube: The c-L1₀ variant was unfavourable for only two of six free surfaces. On the other hand, no L1₀ variant was favourable for the entire sample. As a consequence, a mosaic of a- and b-L1₀ variant domains nucleated at the initial Fe (001) free surface. However, the stability of the initial c-L1₀ variant LRO away from this surface inhibited their growth.

The free surfaces limiting the nanocube effectively stabilized the initial c-variant L1₀ superstructure. The occurrence of this phenomenon is one of the most important conclusions of the present study. Consequently, when compared with other simulated samples, the annealed nanocube showed the highest volume fraction of the initial c-L1₀ variant domains. Besides, the L1₀ domain structure in the nanocube was stable not only in the inner volume, but also in the surface affected regions (see the ESI). The result may be important for the development of the L1₀ nanoparticle matrix technology, which would be structurally more stable than the traditional L1₀-ordered nanolayers.

It is remarkable that all three samples showed identical superstructure stabilities in the inner volumes not affected by the surface induced phenomena. This, in turn, was a consequence of the discontinuous character of those phenomena resulting in sharp APBs separating the inner and surface areas of the samples.

All the above effects were reflected by the character of the ordering of the initially disordered samples.

After long time annealing at $T/T_T = 0.95$ all the samples showed well developed L1₀ atomic long-range order. According to the surface energy relationships described above, the particular free

surface geometries determined the $L1_0$ variants developing in the samples. Consequently, an almost purely a- $L1_0$ -variant superstructure (defected by antiphase boundaries) was observed in the nanowire, and a mosaic of a- and b-variant domains was generated in the nanolayer (Figure 10). No definite selection of the $L1_0$ -variants in the nanocube resulted, in turn, in almost monovariant LRO in the inner part (the particular $L1_0$ -variant selected at random) and a quite high contribution of other $L1_0$ variants close to the surface. The latter was inevitable due to the variant winning inside the cube being always unfavourable for two surfaces. The study of ordering kinetics in the nanocube showed definite, though slow, homogenization of the $L1_0$ superstructure inside the sample – the process obviously driven by the reduction of the APB density.

As revealed by the analysis of MC-time dependence of the values of the 2D correlation parameters $\rho_\alpha^{(hkl)}$ (Equation 4) in the initially disordered nanocube, the $A1 \rightarrow L1_0$ transformation was initiated at the free surfaces (Figure 16) – the result confirming the finding of Mueller et al. [11].

Studies aiming at the elucidation of the effect in terms of the energetics of the simulated system are currently being carried out. At the present stage, two factors are considered: In view of the discontinuous character of the $A1 \rightarrow L1_0$ transformation, creation of an ordered domain in the disordered matrix of FePt means the generation of a sharp $A1/L1_0$ boundary which reduces the system configurational energy gain due to ordering. It is expected that the above effect is reduced if the $L1_0$ domains are created at the surface and the effective $A1/L1_0$ boundary area is reduced. Another effect which should be taken into account is the vacancy formation energy in FePt. This is markedly lower at the surface than in the inner part of a sample. This may prolong the average residence time of the vacancy in the surface parts of the sample and consequently accelerate the chemical ordering occurring via vacancy-mediated atomic jumps.

The detailed analysis of chemical ordering in terms of the stability of particular $L1_0$ superstructure variants in particular nanostructure geometries considerably improves the understanding of the effect of nanostructurization on this phenomenon.

Except for the observation of percolation effects in the ‘thin’ samples, the *rigid lattice* approach showed no significant size effect on the simulated phenomena. The surface nucleation and growth of domains of the favourable $L1_0$ variants – being the basic observed phenomenon – was entirely surface controlled. As previously shown [18,21] the resulting energy gain of the system originated exclusively from the reorientation of the monatomic planes within the surface row of the $L1_0$ supercells and the

further domain growth inward the sample volume proceeded with extremely low driving force resulting in a specific fluctuating kinetics. Consequently, the effective rate of the growth did not depend on the sample thickness. This affected only the time the growing domains needed to percolate across the entire samples.

The results obtained in the present work cannot be useful without a critical survey of the assumptions and approximations applied in the study:

- Use of the *rigid lattice* MC simulations as the main tool for the presented study definitely excluded any insight into the details of surface reconstruction involving modifications/deformations of the crystalline structure. The simulated samples were definitely limited by flat (100)-type surfaces and no atomic jumps beyond these surfaces were possible. This also excluded any surface roughening – e.g. by the formation of adatoms, terraces etc.
- No specific surface potentials were implemented in the simulations. The effective configurational energy of the free surfaces resulted exclusively from breaking the nn and nnn atomic pair-interactions evaluated for the bulk FePt.

It is known that off-lattice MC or MD simulations of surface limited systems modelled with embedded atom potentials or with an ab initio calculation might reveal some spatial relaxation at, and very near, the surface or any interface. If large enough, this might lead to local segregation of the components near the surface or interface and change the stability of the local structures. As remarked earlier, the FePt nanolayer was simulated by means of such techniques [20,21] and the results showed a good agreement with the rigid-lattice ones. It should, however, be admitted that new effects might appear in the case of the nanowires and nanocubes – especially in the size effect area. Despite the above remarks, the methodology applied in the present work finds justification due to: (i) the experimental confirmation of the basic effects (i.e. surface induced nucleation and growth of the domains of favourable $L1_0$ -variants) presumed by the ‘rigid lattice’ MC simulations and (ii) the fact that, in spite of the possible shortcomings, it was the only possible approach making it possible to cover sufficiently long time scale of the process with a reasonable CPU time.

Nevertheless, further studies covering diversely shaped FePt nanoparticles modelled with continuous two- and many-body potentials are presumed in the future.

Acknowledgments

Support is acknowledged from the COST Action MP0903 NANOALLOY. Two of the authors (R.K. and G.E.M.) acknowledge support from the European Community's Seventh Framework Programme (FP7-PEOPLE-2013-IRSES) under EC-GA no. 612552 and from the funds of the Polish Ministry of Science and High Education (Grant no. 3135/7. PR/2014/2). Access to the computation facilities at the ACK Cyfronet AGH, Krakow (supercomputer "Zeus") is greatly appreciated. The authors are also grateful to Dr. Lukasz Zosiak for the valuable assistance at the numerical calculations.

Notes and References

^aM. Smoluchowski Institute of Physics, Jagiellonian University in Krakow, Lojasiewicza 11, 30-348 Krakow, Poland

^bInstitut de Physique et Chimie des Matériaux de Strasbourg, Université de Strasbourg, CNRS UMR 7504, 23 rue du Loess, BP 43, F-67034 Strasbourg, France

^cThe University Centre for Mass and Thermal Transport in Engineering Materials, Priority Research Centre for Geotechnical and Materials Modelling, School of Engineering, The University of Newcastle, Callaghan, NSW 2308, Australia

†This article was submitted as part of a Themed Issue 'Recent advances in the chemical physics of nanoalloys'

‡Electronic supplementary information (ESI) available

1. K. Sato and Y. Hirotsu, *Mater. Trans.*, 2003, **44**, 1518.
2. K. Sato, Y. Hirotsu, *J. Magn. Magn. Mater.*, 2004, **272–276**, 1497.
3. T. Miyazaki, O. Kitakami, S. Okamoto, Y. Shimada, Z. Akase, Y. Murakami, D. Shindo, Y. K. Takahashi and K. Hono, *Phys. Rev. B: Condens. Matter Mater. Phys.*, 2005, **72**, 144419.
4. C.-b. Rong, D. Li, V. Nandwana, N. Poudyal, Y. Ding, Z. L. Wang, H. Zeng and J. P. Liu, *Adv. Mater.*, 2006, **18**, 2984.
5. H. Wang, B.-f. Hua, L. Zhang, M. Li, E. Ja and Z. Liu, *J. Magn. Magn. Mater.*, 2014, **362**, 47.
6. Y. Liu, Y. Jiang, X. Zhang, Y. Wang, Y. Zhang, H. Liu, H. Zhai, Y. Liu, J. Yang and Y. Yan, *J. Solid State Chem.*, 2014, **209**, 69.
7. R. V. Chepulsii and W. H. Butler, *Phys. Rev. B: Condens. Matter Mater. Phys.*, 2005, **72**, 134205.
8. R. V. Chepulsii, J. Velev and W. H. Butler, *J. Appl. Phys.*, 2005, **97**, 10J311.
9. B. Yang, M. Asta, O.N. Mryasov, T.J. Klemmer and R.W. Chantrell, *Acta Mater.* 2006, **54**, 4201.
10. M. Müller and K. Albe, *Phys. Rev. B: Condens. Matter Mater. Phys.*, 2005, **72**, 094203.
11. M. Müller and K. Albe, *Beilstein J. Nanotechnol.*, 2011, **2**, 40.
12. Y J Li, W H Qi, B Y Huang, M P Wang, J F Liu and S Y Xiong, *J. Phys. D: Appl. Phys.*, 2011, **44**, 115405.
13. A. Lyberatos, D. Weller, and G. J. Parker, *J. Appl. Phys.*, 2013, **114**, 233904.
14. S. Zhang, W. Qi and B. Huang, *J. Chem. Phys.*, 2014, **140**, 044328.
15. S. Yamakawa, R. Asahi and T. Koyama, *Surf. Sci.*, 2014, **622**, 65.
16. M. Kozłowski, R. Kozubski, V. Pierron-Bohnes, W. Pfeiler, *Comput. Mater. Sci.*, 2005, **33**, 287.
17. C. Issro, M. Abes, W. Püschl, B. Sepiol, W. Pfeiler, P. F. Rogl, G. Schmerber, W. A. Soffa, R. Kozubski, V. Pierron-Bohnes, *Metall. Mater. Trans. A*, 2006, **37**, 3415.
18. M. Kozłowski, R. Kozubski, Ch. Goyhenex, V. Pierron-Bohnes, M. Rennhofer, S. Malinov, *Intermetallics*, 2009, **17**, 907.
19. M. Rennhofer, M. Kozłowski, B. Laenens, B. Sepiol, R. Kozubski, D. Smeets, A. Vantomme, *Intermetallics*, 2010, **18**, 2069.
20. M. Kozłowski, R. Kozubski, C. Goyhenex, *Mat. Lett.*, 2013, **106**, 273.
21. M. Kozłowski, R. Kozubski, Ch. Goyhenex, in *Diffusion Foundations*, ed. G.E. Murch, A. Oechsner and I.V. Belova, Trans Tech Publications, Switzerland, 2014, Vol. 1, ch.1, pp 3–27.
22. F. Haider, R. Kozubski, T.A. Abinandanan, in: *Alloy Physics. A comprehensive reference.*, ed. W. Pfeiler, Wiley, Weinheim 2007 (ISBN: 978-3-527-31321-1), pp. 667-686
23. A. Dannenberg, M. E. Gruner, A. Hucht, P. Entel, *Phys. Rev. B*, 2009, **80**, 245438.

CP-ART-02-2015-001054.R3

Chemical ordering phenomena in nanostructured FePt: Monte Carlo Simulations

by *S. Brodacka, M. Kozłowski, R. Kozubski, Ch. Goyhenex, G.E. Murch*

Figures with captions

Figure_1.tif

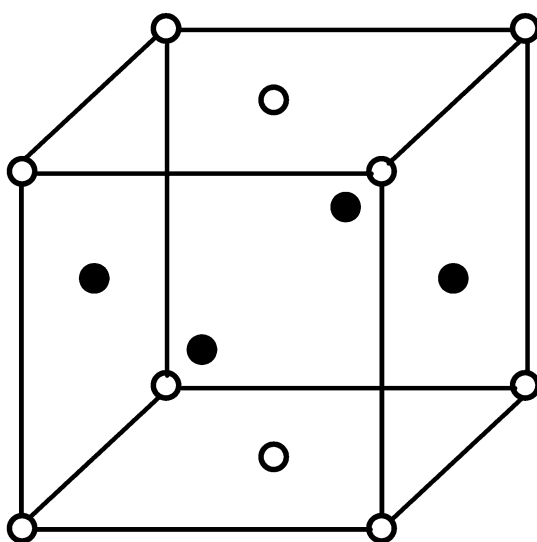
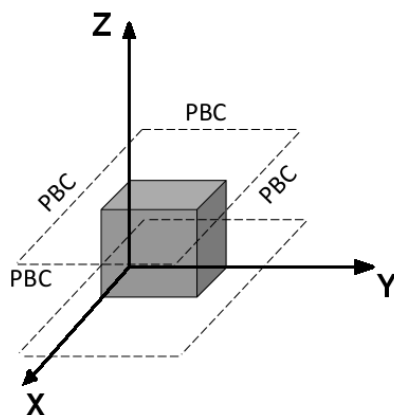
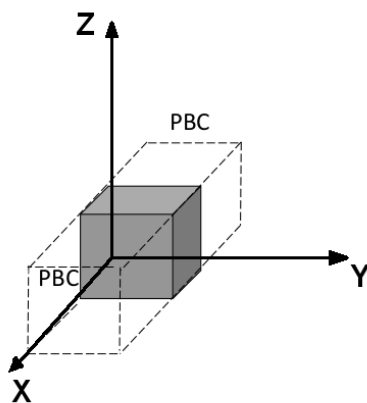


Figure 1 Scheme of the $L1_0$ superstructure of FePt: (●) Fe atoms, (○) Pt atoms. The (100), (010) and (001) orientations of the sequences of alternate Fe and Pt monatomic planes define the a-, b- and c-variants of the $L1_0$ superstructure.

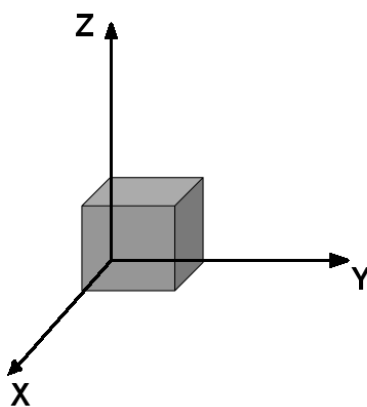
Figure_table1a



Figure_table1b



Figure_table1c



The above figures are inserted in Table 1

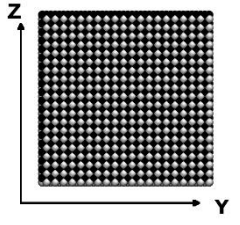
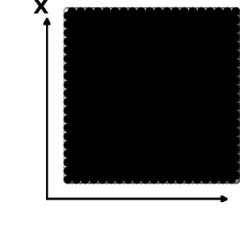
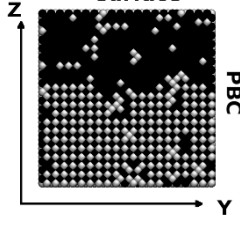
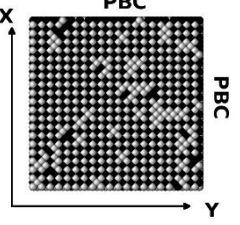
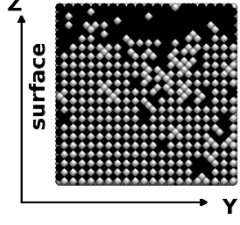
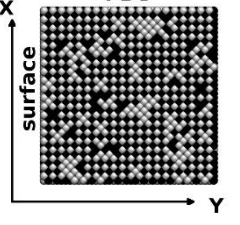
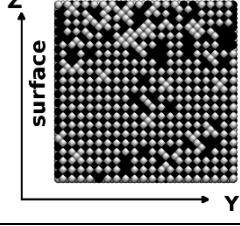
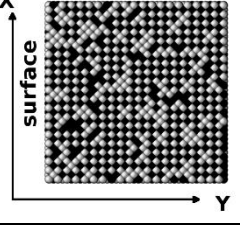
Image type	(100)-oriented cross section	(001)-oriented free surface
Initial configuration: $\eta_a = \eta_b = 0, \eta_c = 1$		
Each sample	Figure_2_a.tiff 	Figure_2_b.tiff 
After 10^{10} MC steps at $T/T_T = 0.95$		
nanolayer	Figure_2_c.tiff surface 	Figure_2_d.tiff PBC 
nanowire	Figure_2_e.tiff surface 	Figure_2_f.tiff PBC surface 
nanocube	Figure_2_g.tiff surface 	Figure_2_h.tiff surface 

Figure 2 Atomic configurations in the ‘thick’ samples initially ordered in the c-L1₀ variant and annealed for 10^{10} MC steps at $T/T_T = 0.95$. Black and white dots represent Fe and Pt atoms, respectively. For the sake of better legibility of the pictures only quarters of the sample cross sections and surfaces.

Figure_3.tiff

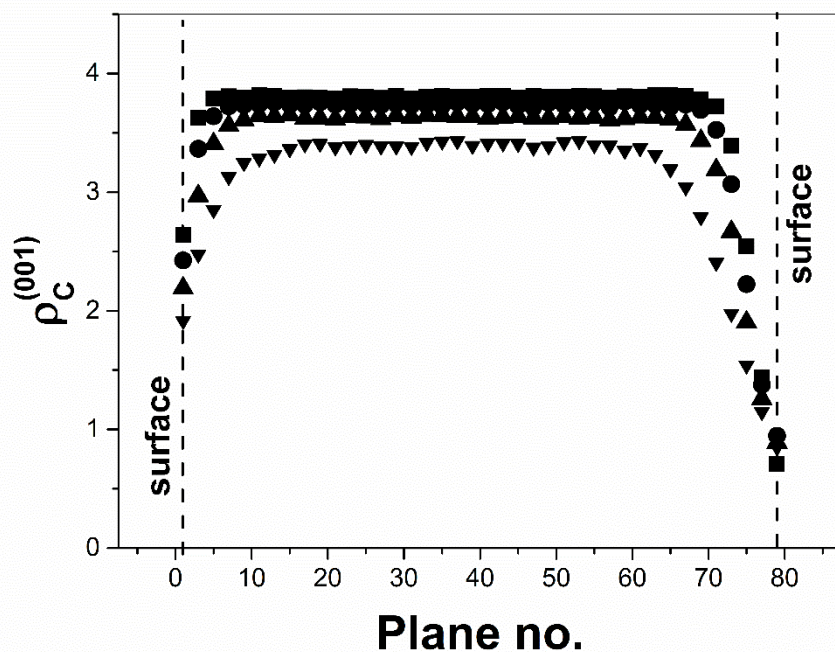


Figure 3 Profiles of $\rho_C^{(001)}$ calculated in the consecutive (001) planes in the nanocube annealed for 10^{10} MC steps at: $T/T_T = 0.76$ (■), $T/T_T = 0.83$ (●), $T/T_T = 0.89$ (▲) and $T/T_T = 0.95$ (▼).

Figure_4.tiff

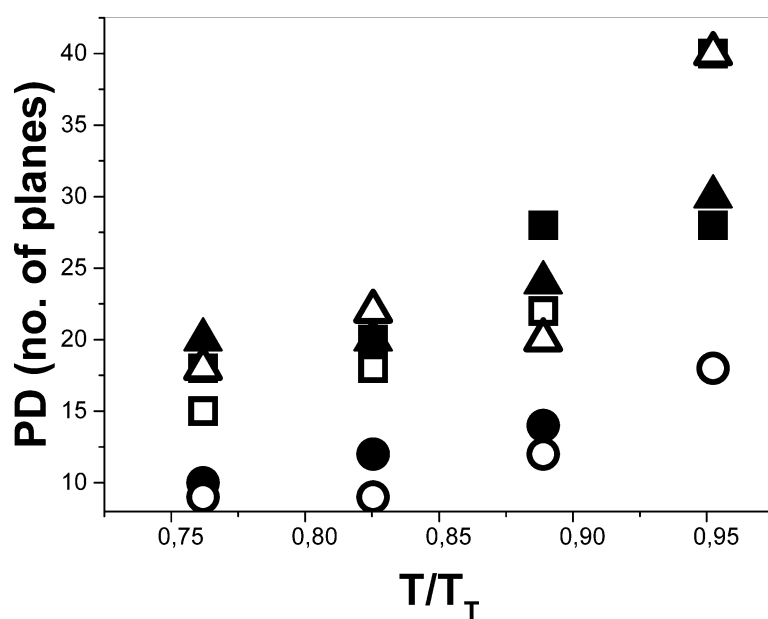


Figure 4 Temperature dependence of the growing domain penetration depth PD in the simulated FePt nanostructures: 'thick' (■) and 'thin' (□) nanolayer; 'thick' (▲) and 'thin' (△) nanowire; 'thick' (●) and 'thin' (○) nanocube.

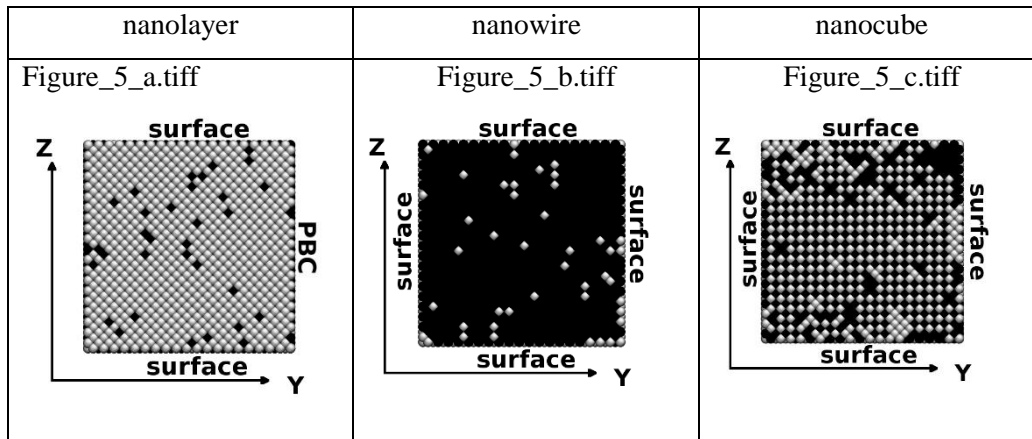


Figure 5 Atomic configurations of the (100) cross sections of the ‘thin’ samples initially ordered in the c-L1₀ variant and annealed for 10¹⁰ MC steps at $T/T_T = 0.95$. Black and white dots represent Fe and Pt atoms, respectively.

Figure_6.tiff

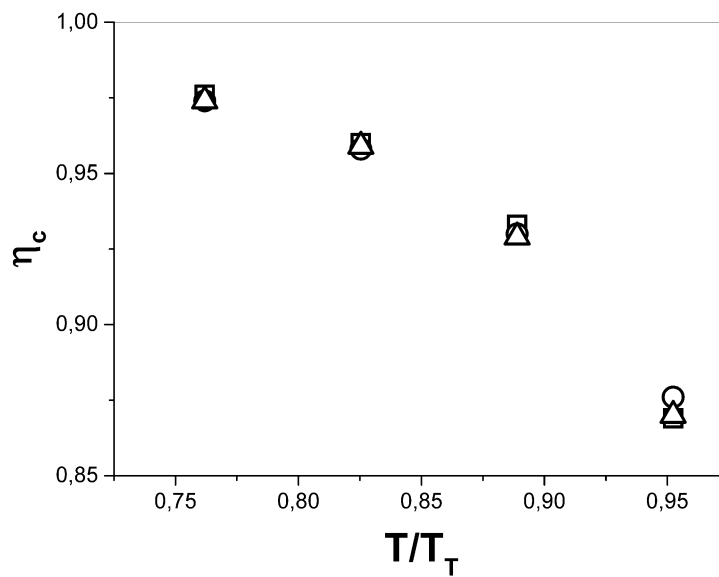


Figure 6 Temperature dependences of the values of η_c in the inner part of the ‘thick’ nanolayer (□), ‘thick’ nanowire (○) and ‘thick’ nanocube (△) after 10¹⁰ MC steps.

Figure_7.tiff

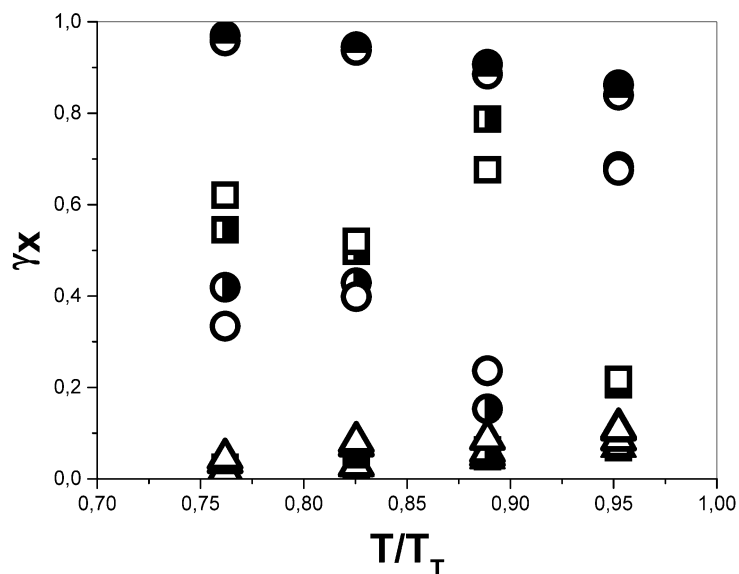


Figure 7 Temperature dependence of the L1₀-variant volume fractions γ_x in a single sample of the 'thick' nanowire. Inner part: γ_a (■), γ_b (▲), γ_c (●); layer adjacent to the (010) surface: γ_a (□), γ_b (△), γ_c (○); layer adjacent to the (001) surface: γ_a (□), γ_b (△), γ_c (○); [100] oriented edge area: γ_a (□), γ_b (△), γ_c (○).

Figure_8.tiff

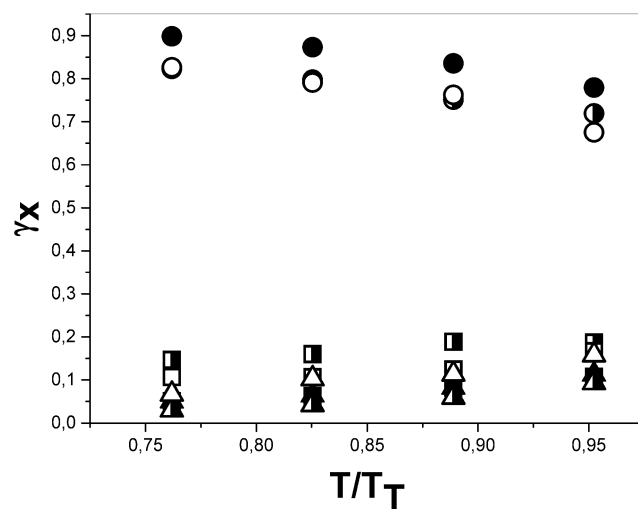


Figure 8 Temperature dependence of the L1₀-variant volume fractions γ_x calculated for the entire sample volume. γ_a : (□)-nanolayer, (■)-nanowire, (■)-nanocube; γ_b : (△)-nanolayer, (▲)-nanowire, (▲)-nanocube; γ_c : (○)-nanolayer, (●)-nanowire, (●)-nanocube.

Figure_9.tiff

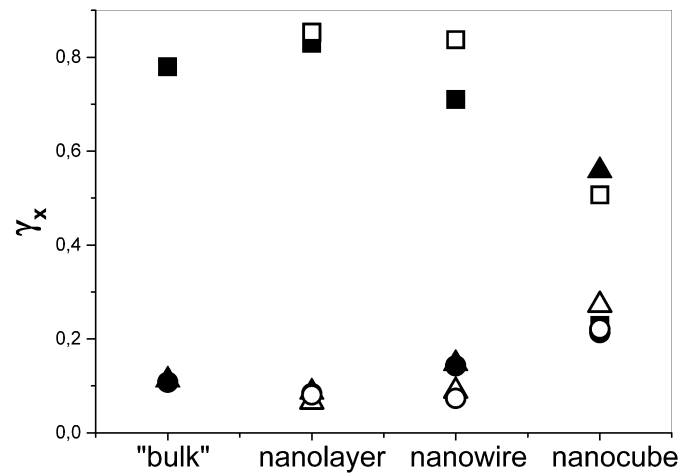


Figure 9 $L1_0$ -variant domain structures of the (001) surfaces of the examined FePt nanostructures after 10^{10} MC steps at $T/T_T = 0.95$: γ_a (■, □); γ_b (▲, △); γ_c (●, ○). Solid and open symbols correspond to the 'thick' and 'thin' samples, respectively. The values of γ_x were obtained by single simulation runs.

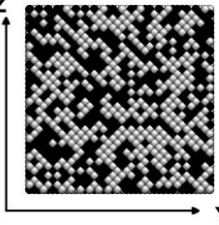
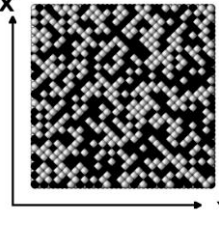
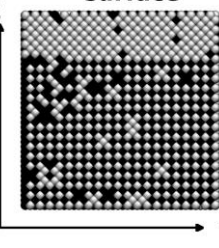
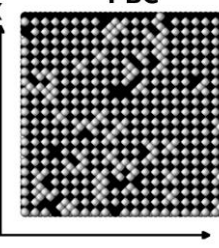
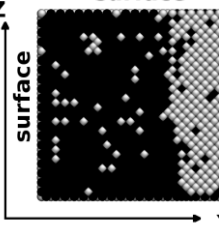
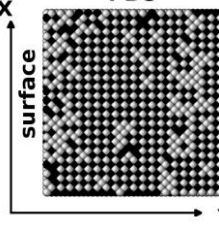
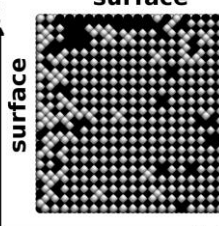
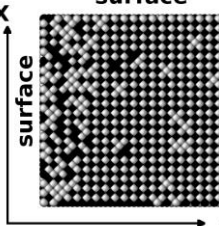
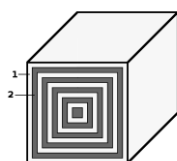
Image type	(100)-oriented cross section	(001)-oriented free surface
Initial configuration: $\eta_\alpha = 0$		
Each sample	Figure_10_a.tiff 	Figure_10_b.tiff 
After 10^{10} MC steps at $T/T_T = 0.95$		
nanolayer	Figure_10_c.tiff surface 	Figure_10_d.tiff PBC 
nanowire	Figure_10_e.tiff surface 	Figure_10_f.tiff PBC 
nanocube	Figure_10_g.tiff surface 	Figure_10_h.tiff surface 

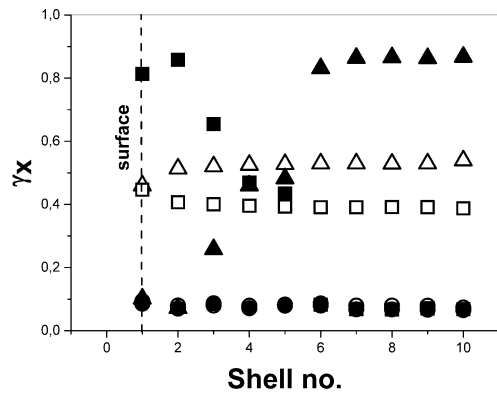
Figure 10 Atomic configurations in initially disordered ‘thick’ samples annealed for 10^{10} MC steps at $T/T_T = 0.95$. Black and white dots represent Fe and Pt atoms, respectively. For the sake of better legibility of the pictures only quarters of the sample cross sections and surfaces are displayed.



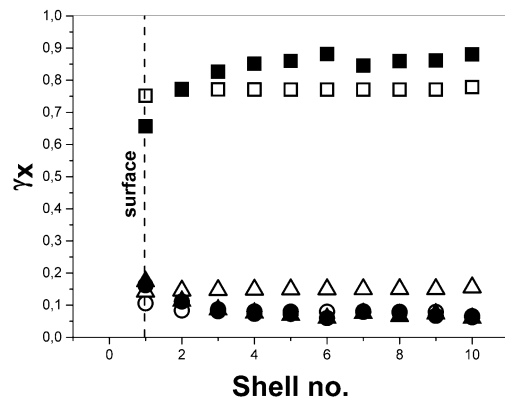
Figure_table_5.tiff

Figure inserted in Table 5

Figure_11_a.tiff



Figure_11_b.tiff



Figure_11_c.tiff

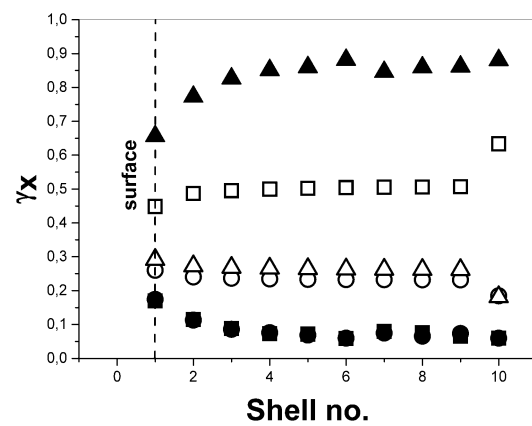


Figure 11 L1₀-variant volume fractions γ_x against the consecutive shell numbers in the initially disordered ‘thick’ FePt nanolayer (a), nanowire (b) and nanocube (c) annealed for 10^{10} MC steps at $T/T_T = 0.95$. γ_a : (■)-single sample, (□)-averaged; γ_b : (▲)-single sample, (△)-averaged; γ_c : (●)-single sample, (○)-averaged.

Figure_12.tiff

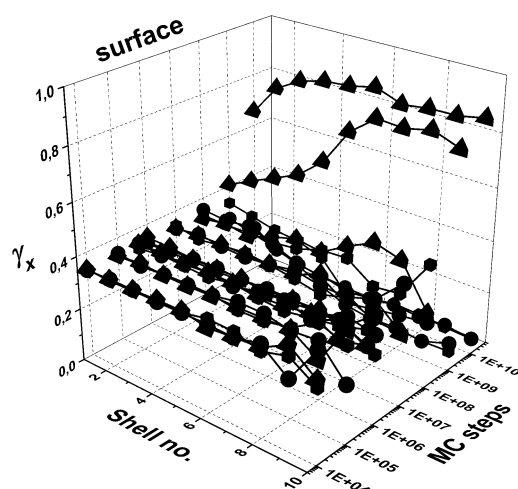


Figure 12 L₁₀-variant volume fractions γ_x against consecutive shell numbers and MC time in initially disordered single 'thick' FePt nanocube: (■) γ_a ; (▲) γ_b ; (●) γ_c .

Figure_13.tiff

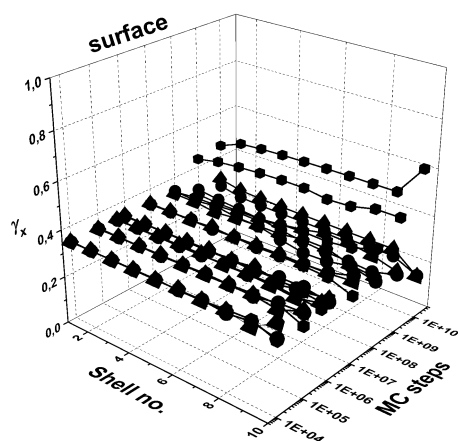


Figure 13 L₁₀-variant volume fractions γ_x against consecutive shell numbers in initially disordered 'thick' FePt nanocube. Data averaged over 30 independent simulation runs: (■) γ_a ; (▲) γ_b ; (●) γ_c .

Figure_14.tiff

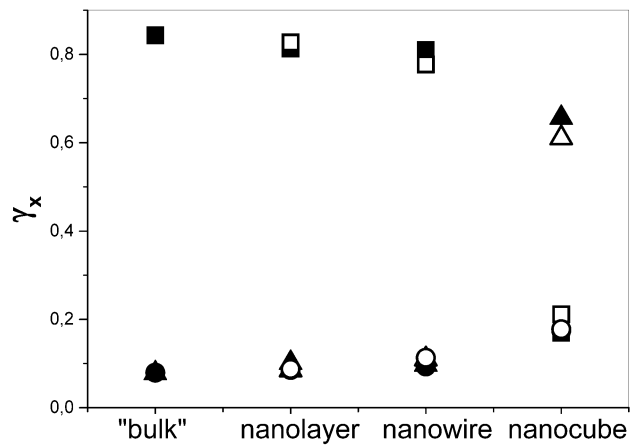


Figure 14 $L1_0$ -variant domain structures of the entire surfaces of the initially disordered FePt nanostructures after 10^{10} MC steps at $T/T_T = 0.95$: γ_a (■, □); γ_b (▲, △); γ_c (●, ○). Solid and open symbols correspond to the 'thick' and 'thin' samples, respectively. The values of γ_x were obtained by single simulation runs.

Figure_15.tiff

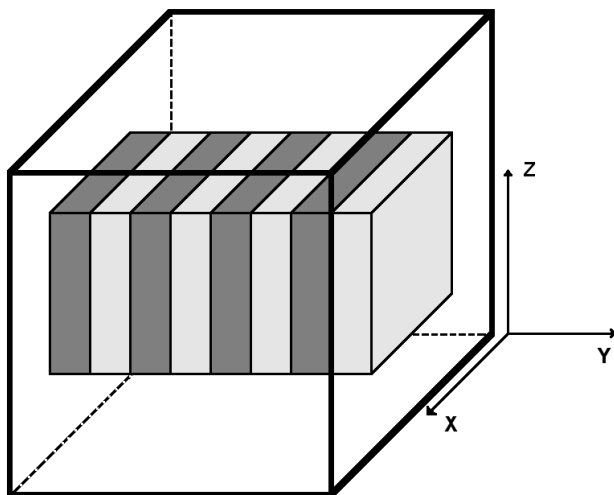


Figure 15 [010]-oriented 'chimney': area for the calculation of $\rho_\alpha^{(010)}$ traced in Figure 16.

Figure_16.tiff

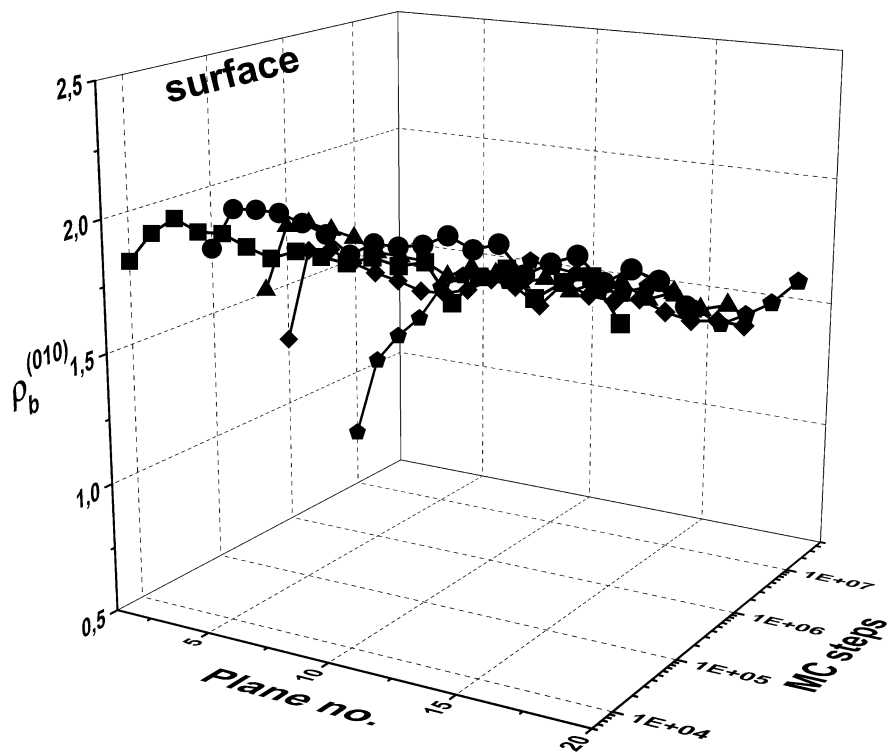


Figure 16 $\rho_b^{(010)}$ in initially disordered single FePt nanocube against the numbers of consecutive (010)-planes in the [010]-oriented 'chimney' shown in Figure 15. (■) 10^4 MC steps, (▲) 10^5 MC steps, (●) 5×10^5 MC steps, (▼) 10^6 MC steps, (◆) 10^7 MC steps.